RESEARCH ARTICLE

CHEMISTRY

Photochromic radical states in three-dimensional covalent organic frameworks with zyg topology for enhanced photocatalysis

Tian-Tian Ma[1,†], Guo-Zhang Huang[2,†], Xiao-Han Wang[1,†], Yan Liang[1], Run-Han Li[1], Bin Wang[1], Su-Juan Yao[1], Jia-Peng Liao[1], Shun-Li Li[1], Yong Yan[1,*] and Ya-Qian Lan[1,*]

[1]School of Chemistry, South China Normal University, Guangzhou, Guangdong 510006, China;

[2]Department of Chemistry, Guangdong Provincial Key Laboratory of Catalytic Chemistry, Southern University of Science and Technology, Shenzhen 518055, China.

*Corresponding authors. E-mails: yong.yan@m.scnu.edu.cn; yqlan@m.scnu.edu.cn

[†]Equally contributed to this work.

Abstract

Covalent-organic frameworks (COFs) with photoinduced donor-acceptor (D-A) radical pairs show enhanced photocatalytic activity in principle. However, achieving long-lived charge separation in COFs proves challenging due to the rapid charge recombination. Here, we develop a novel strategy by combining [6 + 4] nodes to construct **zyg**-type 3D COFs, first reported in COF chemistry. This structure type exhibits a fused Olympic rings-like shape, which provides a platform for stabilizing the photoinduced D-A radical pairs. The **zyg**-type COFs containing catalytically active moieties such as triphenylamine and phenothiazine (PTZ) show superior photocatalytic production rates of hydrogen peroxide (H_2O_2). Significantly, the photochromic radical states of these COFs show up to 400% enhancement in photocatalytic activity compared to the parent states, achieving a remarkable H_2O_2

© The Author(s) 2024. Published by Oxford University Press on behalf of China Science Publishing & Media Ltd. This is an Open Access article distributed under the terms of the Creative Commons Attribution License (http://creativecommons.org/licenses/by/4.0/), which permits unrestricted reuse, distribution, and reproduction in any medium, provided the original work is properly cited.

ORIGINAL UNEDITED MANUSCRIPT

Downloaded from https://academic.oup.com/nsr/advance-article/doi/10.1093/nsr/nwae177/7679147 by guest on 24 May 2024

synthesis rate of 3324 μmol g^{-1} h^{-1}, which ranks the PTZ-COF one of the best in crystalline porous photocatalysts. This work would shed light on the synthesis of efficient 3D COF photocatalysts built on topologies which can facilitate photo-generating D-A radical pairs for enhanced photocatalysis.

Keywords: three-dimensional covalent-organic frameworks, photochromic radical states, donor and acceptor, hydrogen peroxide, photocatalysis.

INTRODUCTION

The photoinduced electron-transfer (PET) process plays an important role in the field of chemistry and biology exemplified by enzymatic catalysis [1], artificial photosystems [2], solar energy conversion [3], among others [4,5]. Searching for new PET systems to produce long-lived charge separation states is crucial for the development of functional materials, especially photocatalysts. The charge separation in PET systems typically involves a redox process within the electron donor-acceptor (D-A) pairs, resulting in separated photoinduced radicals which possess stronger reducing or oxidizing ability and enhanced light absorption in principle compared with their neutral parent states [6–8]. The generation of photochromic radical states (PRSs) with lifetime ranging from hours to days has been achieved in hybrid materials [9,10], supramolecular assemblies [11], metal-organic frameworks (MOFs) [12], hydrogen-bonded organic frameworks (HOFs) [13] and organic polymers [14], but still absent in covalent organic frameworks (COFs). COFs have emerged as a new class of highly designable and tailorable crystalline porous organic skeletons with periodically ordered structures, showing great potential in heterogeneous catalysis on account of their high stability and porosity [15–18]. Thus, it is a crucial research direction to construct COF materials with PRSs in order to exploit the full extent of the photocatalytic performance.

In the previously reported COFs, only sub-second lifetime of the photoinduced charge separation (PCS) state can be reached [19–21]. The stabilization of long-lived charge separation states in COFs is confronted with two major challenges: one is to

ORIGINAL UNEDITED MANUSCRIPT

Downloaded from https://academic.oup.com/nsr/advance-article/doi/10.1093/nsr/nwae177/7679147 by guest on 24 May 2024

ensure the effective PET within the D-A pairs and the other is the inhibition of reversed charge recombination. In view of Marcus-Hush theory [22,23], regarding to the former, distinct electron donating/accepting properties, suitable molecular orbit arrangement and close-in contact of the D-A pairs are required for an effective electron jumping while the latter prefers rather remote distance between the D-A pairs to prevent recombination. This means that building units with proper length are required for constructing such photochromic COFs. In view of the reticular chemistry [24,25], compared with the layer-by-layer stacking of two-dimensional (2D) COF structures, the three-dimensional (3D) interconnection of the building units in 3D COFs can afford more pathways for ET and stabilize separated photoinduced charges through stronger electrostatic attraction interactions. In addition, 3D COFs with meso-porosity (with pore diameter larger than 2 nm) [26] can usually accommodate more accessible donor and acceptor sites with good catalytic activity [27]. Thus, 3D COF systems with suitable periodically ordered building blocks would be potential molecular platforms for photogeneration of metastable charge separation radical states (Fig. 1a). Since the discovery of COFs by Yaghi in 2005 [15], most of the work has focused on the exploration of 2D structures and a fraction of 3D COFs were designed and synthesized [16,28,29]. In the 3D COFs database, the 4-connected building blocks with tetrahedral (T_d) symmetry were mostly used to connect with other building units in [4 + 2], [4 + 3] and [4 + 4] modes to form topologies such as **dia**, **bor** and **pts** in the early studies [30–32]. In recent years, 3D COFs based on higher connectivity building units have been synthesized with new topologies featuring [6 + 2], [6 + 3], [6 + 4], [6 + 6], [8 + 2], or [8 + 4] nets [25]. Among these, 3D COF structures based on [6 + 4] net were constructed showing high surface area, high structural stability, absence of structural interpenetration and decent catalytic properties. However, for [6 + 4]-connected COFs, only four topologies–**hea**, **soc**, **stp** and **she** assembled by linking 6-connected building units with T_d and square nodes have been reported, respectively (Fig. 1b) [33–36].

Triphenylamine (TPA) and phenothiazine (PTZ) are well-known electron-rich functional groups with distinct features, such as strong electron-donating characteristics, tunable redox properties and versatility of functionalization, meaning that they cater well to our purpose acting as PCS state 3D COF building units [37–39]. Herein, we have extended the triangular TPA and PTZ groups into (3,3)-type six-connected building blocks, forming an irregular hexagon. Combining these

ORIGINAL UNEDITED MANUSCRIPT

Downloaded from https://academic.oup.com/nsr/advance-article/doi/10.1093/nsr/nwae177/7679147 by guest on 24 May 2024

designed hexagonal building units (hexa-CHO) with a planar quadrilateral building block (tetra-NH_2), we have synthesized a family of (3,3,4)-connected 3D COFs with **zyg** topology, which has been previously observed in MOFs but only is first reported in COFs [40]. It is noteworthy that two types of one-dimensional pores and an Olympic rings-like shape are observed in the crystallographic axis *c* direction in the **zyg**-type 3D COFs. The rare multi-sized one-dimensional pores have the potential to further increase the specific surface area, as well as to carry out some domain-limited catalytic reactions. This is the first 3D COF with a fused Olympic rings shape synthesized in COF structures. Most importantly, the metastable PCS radical states were obtained through light irradiation in the TPA and PTZ-based COFs, confirmed by the photochromic phenomenon and electron paramagnetic resonance characteristics. To further investigate more inherent impacts PCS bring to the COF materials, various photoelectrochemical characterizations were conducted revealing that light harvest ability and carrier transport capacity were both enhanced for the metastable radical states of the **zyg** COFs. In addition, TPA- and PTZ-based COFs often show high crystallinity which can improve the photoelectron generation and transfer within the lattice [41]. H_2O_2 is used as a green, clean and storable oxidant in a wide range of applications such as medical disinfection, paper bleaching and organic synthesis [42]. Herein, the TPA and PTZ-based COFs were applied to the photocatalytic synthesis of hydrogen peroxide (H_2O_2), showing significant catalytic activity improvement for the metastable radical states (>200% enhancement for TPA COF and >400% for PTZ COF compared with the as-prepared samples) and the highest H_2O_2 photosynthesis rate reaches 3324 μmol g^{-1} h^{-1} for the activated PTZ-based COF, ranking one of the best porous crystalline photocatalysts in H_2O_2 photosynthesis. This work has successfully constructed metastable charge separation radical states in COFs of **zyg** topology for the first time and enhanced the catalytic performance by several orders of magnitude, providing an effective strategy on catalytic activity enhancement for 3D COF materials.

RESULTS AND DISCUSSION

Synthesis and characterizations

In order to construct new [6 + 4]-connected COFs, as shown in Fig. 2, hexa-aldehyde precursors containing functionalized central cores acting as strong electron donors

ORIGINAL UNEDITED MANUSCRIPT

Downloaded from https://academic.oup.com/nsr/advance-article/doi/10.1093/nsr/nwae177/7679147 by guest on 24 May 2024

(TPA-6CHO, PTZ-6CHO) and weak ones (Ph-6CHO, TPB-6CHO) were used. The crystalline products, named **M-COF**, **N-COF**, **S-COF**, and **T-COF**, can be obtained through the Schiff condensation reaction using the above aldehydes and dimethyl functionalized tetra-amine (TAPB-Me). These COF materials were synthesized in yields ranging from 60% to 70% via solvothermal method where the reactant monomers were heated at 120 °C in a mixture containing *o*-dichlorobenzene, dichloromethane, and trifluoroacetic acid for 3 days (see the Supplementary Information for more details). The resulting four COFs were insoluble in common organic solvents such as dimethyl sulfoxide (DMSO), acetone and methanol (Figs S1 and S2, see Supplementary Information).

The structures of these 3D COFs were unambiguously characterized using various analytical methods. Solid-state ^{13}C cross-polarization magic angle spinning (CP/MAS) NMR spectra (Figs S3–S6) verified the presence of the imine moiety showing peaks at ~160 ppm. Considering that monomers with multiple reaction sites may give sub-stoichiometric 3D COFs due to under reactivity, in order to quantitatively determine the ligand ratios, these COFs were decomposed and dissolved using DCl/DMSO-d_6 and analyzed by solution-state ^1H NMR (Figs S7 and S8). The ratios of amino and aldehyde precursors in both **N-COF** and **S-COF** were close to 3:2. This stoichiometry is consistent with the that observed in the crystal structure models. The Fourier transform infrared (FT-IR) spectra of **M-COF**, **N-COF**, **S-COF** and **T-COF** (Figs S9–S12) show the formation of imine bond (1623 cm^{-1}) and the disappearance of C–O vibration of the aldehyde group (1698 cm^{-1}) and the N–H vibration of the amino group (3352 cm^{-1}). Thermogravimetric analysis (TGA) (Fig. S13) was performed under N_2 atmosphere to assess the thermal stability, and these 3D COFs were stable up to 450 °C before being decomposed. Field emission scanning electron microscopy (FE-SEM) images (Fig. 3a and Fig. S14) reveal that all these COFs show defined hexagonal-shaped nanocrystals.

Crystalline structure and porosity

Measurements of powder X-ray diffraction (PXRD) combined with theoretical structural simulations were used to elucidate the crystal structures of the above COFs. The structural models for all these COFs were established based on **zyg** topology in $P6_3/mcm$ space group. As shown in Fig. 2c, the experimental PXRDs for these four COFs exhibit the first strongest peaks at 2.40°, 2.14°, 2.20° and 2.04°, respectively,

ORIGINAL UNEDITED MANUSCRIPT

Downloaded from https://academic.oup.com/nsr/advance-article/doi/10.1093/nsr/nwae177/7679147 by guest on 24 May 2024

which are attributed to the (010) planes of the hexagonal unit cells. The calculated PXRD patterns of the geometrically optimized structures are in good agreement with the experimental results. Full profile Pawley refinements were performed to obtain the unit cell parameters ($a = b = 42.39$ Å, $c = 9.15$ Å, $R_p = 5.5\%$, $R_{wp} = 7.6\%$ for **M-COF**; $a = b = 47.65$ Å, $c = 9.65$ Å, $R_p = 5.1\%$, $R_{wp} = 7.2\%$ for **N-COF**; $a = b = 46.87$ Å, $c = 9.26$ Å, $R_p = 5.8\%$, $R_{wp} = 6.9\%$ for **S-COF**; $a = b = 50.08$ Å, $c = 8.91$ Å, $R_p = 6.2\%$, $R_{wp} = 8.4\%$ for **T-COF**), which led to satisfactorily low residual values and acceptable profile differences. Also, Rietveld refinements based on the **zyg**-type structural models for these COFs against the PXRD data revealed good match between the calculated and experimental patterns (Figs S15–S22), confirming the model structures. According to the Reticular Chemistry Structure Resource (RCSR) [24], combining a potential co-planar 6-connected node with a square building block can also form the **rht**-network which has been observed in a series $\{Cu_2(COO)_4\}$ paddlewheel-based metal-organic frameworks [43–45]. Therefore, as an example, the crystal structure for **N-COF** was also modeled based on **rht** topology where the three branched isophthalaldehyde of the hexa-CHO are on the same plane. However, the calculated PXRD pattern does not match with the experimental one (Fig. S23), which rules out the possibility for for these COFs to adopt **rht** topology. In addition, the [6 + 4]-connected network with **stp** topology showing the same hexagonal symmetry as the **zyg**-net has been tested for the structural modeling of **N-COF**. The structure of **N-COF-stp** shows a significantly larger unit cell (space group: P_6, $a = 52.30$ Å, $c = 13.88$ Å) than the one provided by the indexing of the experimental PXRD pattern, suggesting the network of **N-COF** adopts **zyg** topology rather than **stp** (Fig. S24). Furthermore, the crystallinity and periodic porous structures of these COFs were also evidenced by high-resolution transmission electron microscopy (HR-TEM) (Fig. 3b–f and Figs S25–S27). The HR-TEM images for **M-COF**, **N-COF**, and **S-COF** all clearly reveal long-range structural ordering consisting of hexagonal honeycomb lattices viewed from [001] direction. The periodic bright spots in these images associate with the larger empty pore channels of these COF structures. The corresponding inverse fast Fourier transform (IFFT) denoised images clearly show lattice fringes with distances of 3.80 nm for **M-COF**, 3.94 nm for **N-COF** and 4.20 nm for **S-COF**, matching well with the d-spacings of [100] lattice planes in these **zyg**-type frameworks. Micro electron diffraction (MicroED) experiments were also conducted on these COF nanocrystals in order to obtain the single crystal structures

ORIGINAL UNEDITED MANUSCRIPT

Downloaded from https://academic.oup.com/nsr/advance-article/doi/10.1093/nsr/nwae177/7679147 by guest on 24 May 2024

for these COFs. However, These COF samples showed barely diffraction spots for single crystal structure solution from MicroED (Fig. S28).

In the construction of the **zyg** net, the TAPB-Me unit acts as a square building block, in which the four branched phenyl rings are almost perpendicular to the central phenyl ring (Fig. 4a). The tetra-amine TAPB (1,2,4,5-tetrakis-(4-aminophenyl)benzene) without methyl groups was also tried to react with the same hexa-aldehydes, but no crystalline products were obtained, suggesting the important role of the two methyl groups in TAPB-Me for directing the formation of the **zyg**-type frameworks. In these **zyg**-type COFs, the three branched isophthalaldehyde rings of the hexa-CHO are not on the same plane, but with a small twist between the branched ring and the central phenyl ring (ie, ~14° for **M-COF**, Fig. 4c). The **zyg**-COFs can be seen in the unit cell *c* direction with two different sizes of pores, both of which can be simplified into hexagons (Channel A and B as shown in Fig. 4a and c, respectively). The irregular hexagon of Channel A is formed by two hexa-CHO units and two TAPB-Me moieties as the edges. Channel B is composed of six TAPB-Me units as edges connected with six isophthalaldehyde units as vertices to form a regular hexagon. Therefore, changing the size of the hexa-CHO building block affects the size of the Channel A. The crystal structure of the expanded **M-COF** shows that the **zyg** network exhibits the shape of a fused Olympic rings in the unit cell *c* axis (Fig. 4b). By varying the size of the hexa-CHO unit, the above four **zyg**-type COFs show different sizes of fused Olympic rings. To investigate the porosity of these 3D COFs, nitrogen adsorption analysis was performed at 77 K after activation of the materials under vacuum (Fig. 2d). The adsorption curves all exhibited typical type *IV* isotherms, showing both microporous and mesoporous properties. The surface areas for these COFs were calculated to be 1226 (**M-COF**), 1696 (**N-COF**), 1383 (**S-COF**), and 891 $m^2\ g^{-1}$ (**T-COF**) according to the Brunauer-Emmett-Teller (BET) theory (Figs S29–S32). Based on the nonlocal density function theory (NLDFT), these COFs have corresponding pore size distribution peaks near 1.0 and 3.4 nm, which are essentially similar to the pore sizes expected from their crystal structures.

Photophysical properties

The structure feature of these COFs provides a geometric platform for stabilizing the charge separation states in 3D lattice. Therefore, PCS in these COFs was investigated. First, the as-prepared COFs were irradiated by Xe-lamp to induce the ET within the

ORIGINAL UNEDITED MANUSCRIPT

Downloaded from https://academic.oup.com/nsr/advance-article/doi/10.1093/nsr/nwae177/7679147 by guest on 24 May 2024

COF. All the COF samples showed photochromism hence solid-state electron paramagnetic resonance (EPR) spectra were collected before and after light irradiation. When irradiating solid samples or samples dispersed in solution, only subtle increasement of the EPR signals around *g*-value of 2.0 was observed for **M-COF** and **T-COF** after light activation, indicating inefficient electron transfer or rapid charge recombination in them (Fig. 5a, b and Figs S33, S34). The EPR signals obviously emerged for the photo-activated samples of **N-COF** and **S-COF**, namely **N-COF*** and **S-COF***, suggesting that the effective ET process occurred and metastable PCS states formed inside **N-COF** and **S-COF** (Fig. 5a, b and Figs S35, S36). The electronic properties of **N-COF** and **S-COF** as well as their activated samples were subsequently investigated via various measurements. The yellow color samples of **N-COF** and **S-COF** showed slightly different photon capture ability, as revealed by their UV-Vis diffuse reflectance spectra (DRS). As seen in Fig. 5c, both **N-COF** and **S-COF** show broad absorption bands with maximum peaks at 380 nm and **S-COF** possesses better visible-light harvesting properties with a 50 nm wavelength red shifting. The change on UV-Vis DRS mainly results from the introduction of phenothiazine group, increasing the conjugation property in the structure. The DRS also revealed that the metastable states **N-COF*** and **S-COF*** possess better visible light absorption ability, resulting from the radical feature of these activated states. By analyzing the T_{auc} plots of $(\alpha hv)^2$ *vs.* photon energy (Fig. 5d), the band gaps E_g were obtained to be 2.74 eV, 2.44 eV for **N-COF** and **S-COF** and 2.55 eV, 2.40 eV for **N-COF*** and **S-COF***, respectively. For the purpose of verifying the energy band positions, Mott-Schottky (M-S) electrochemical measurements were also carried out. Based on the M-S results (Figs S37–S40), the HOMO positions of **N-COF**, **S-COF** and their corresponding activated structures were calculated to be −0.60, −0.65, −0.63 and −0.62 eV, respectively. On the basis of the equation $E_g = E_{VB} - E_{CB}$, the LUMO positions of **N-COF**, **S-COF**, **N-COF*** and **S-COF*** were calculated to be 2.14, 1.79, 1.92 and 1.78 eV, respectively. As shown in Fig. 5f, the band structures of **N-COF** and **S-COF** before and after activation were adequate for the synthesis of H_2O_2 from H_2O (E (H_2O_2/H_2O) = +1.78 V *vs* NHE) and O_2 (E (O_2/H_2O_2) = +0.68 V *vs* NHE), indicating that these COFs can be suitable for the catalytic synthesis of H_2O_2.

ORIGINAL UNEDITED MANUSCRIPT

Downloaded from https://academic.oup.com/nsr/advance-article/doi/10.1093/nsr/nwae177/7679147 by guest on 24 May 2024

It can be inferred above that the light activation of **N-COF** and **S-COF** samples increased the photon capture abilities and meanwhile narrowed the energy band gaps. To further understand the impacts PCS state brought to these two COFs, the transient photocurrent response was measured to evaluate the photogenerated carrier separation efficiency and the charge transport capacity. The transient-photocurrent-response intensity of **S-COF** was slightly larger than that of **N-COF** under visible light ($\lambda >$ 420 nm). When illuminating **N-COF** and **S-COF** with Xe lamp without any optical filter, the photocurrent would show intensity enhancement with illumination time increasing, meaning that the PCS states for these COFs bring benefits on the photogenerated carrier separation efficiency and the charge transport capacity, and this trend is more significant for **S-COF** than **N-COF** (Fig. 5e and Figs S41, S42).

Photocatalytic synthesis of H_2O_2

Compared to the industrial anthraquinone oxidation method, the photocatalytic synthesis of H_2O_2 is safer and more environmentally friendly by utilizing renewable solar energy and clean resources (H_2O and O_2) [42,46]. Currently, organic polymer-based photocatalysts such as graphitic carbon nitride (g-C_3N_4) has been widely applied in the photocatalytic production of H_2O_2 [47,48]. However, their further development has been hindered by the unsatisfactory catalytic activity due to the low crystallinity and poor photogenerated carrier separation. Since 2020, COFs have arisen as an ideal candidate for the H_2O_2 photosynthesis because of their well-defined structures, excellent stability and desired semiconductor-like behavior [46,49]. Although the light absorption ability of these COFs is quite moderate, the fine photogenerated carrier separation efficiency and the charge transport capacity as well as the suitable arrangement of the acceptor-donor pairs make them possible to be used as highly efficient photocatalysts. Therefore, **N-COF** and **S-COF** containing photo-catalytically active groups (TPA and PTZ) were tested for the synthesis of H_2O_2 (Figs S43–S48). First, the photocatalytic activity of the reported COFs was evaluated by photocatalytic oxygen reduction reaction (ORR) for the H_2O_2 production under Xe lamp irradiation using isopropanol as sacrificial reagent. The photosynthetic rates of H_2O_2 in 10% isopropanol aqueous solution are 560 and 596 μmol g^{-1} h^{-1} for **N-COF** and **S-COF**, respectively, while the values increased to 794 and 1474 μmol g^{-1} h^{-1} for **N-COF*** and **S-COF*** (Fig. 6a). The enhancement of the photocatalytic performance might result from the better photon capture ability, photogenerated carrier separation

ORIGINAL UNEDITED MANUSCRIPT

Downloaded from https://academic.oup.com/nsr/advance-article/doi/10.1093/nsr/nwae177/7679147 by guest on 24 May 2024

efficiency and the charge transport capacity for the PCS radical samples. The much more dramatic increasing of activity for the activated **S-COF** compared with **N-COF** can be attributed to the increasing of conjugation property because of the phenothiazine group. Subsequently, the H_2O_2 photocatalytic synthesis with Xe lamp was also conducted in pure water, displaying H_2O_2 photosynthetic rates of 656, 450, 710 and 1160 μmol g^{-1} h^{-1} for **N-COF**, **S-COF**, **N-COF*** and **S-COF***, respectively (Fig. 6a). There was a clear accumulation of the H_2O_2 yield with the increasing of irradiation time, displaying close linear relationship between H_2O_2 production and irradiation time for all the above COFs, suggesting that the high photosynthetic rates could remain even with a long irradiation time (Fig. 6b). This provides proof for the fact that the light-activated states were quite stable even in catalytic reaction condition. Furthermore, in consideration of the moderate visible light absorption of these COFs, we also conducted the photocatalytic H_2O_2 production using a 380 nm of LED light as the monochromatic illuminant. It showed H_2O_2 photosynthetic rates of 491, 759, 1140 and 3324 μmol g^{-1} h^{-1} for **N-COF**, **S-COF**, **N-COF*** and **S-COF***, respectively (Fig. 6a). It is worth noting that **S-COF*** showed dramatic enhancement in photocatalytic activity, up to four times compared with the parent **S-COF**. Although recently Liao et al. reported pyrazine-functionalized COFs with the highest photocatalytic H_2O_2 production rate of 7327 μmol g^{-1} h^{-1} in COF photocatalysts [50], the H_2O_2 synthesis rates of most reported COFs are quiet moderate [46]. Thanks to the activity enhancement resulting from the PCS state, the excellent photocatalytic performance of **S-COF*** makes it one of the best porous crystalline photocatalysts upon H_2O_2 production (as listed in Table S1). The cycling stability tests were also carried out to evaluate the durability of the photocatalyst for **N-COF*** and **S-COF***, showing slightly decreasing catalytic performance after three cycles of photocatalytic tests (Fig. 6c). These results have evidenced that the PCSs in these COFs were very stable with a substantially long lifetime.

Photocatalytic mechanism studies

To investigate the mechanism of the photocatalytic H_2O_2 production for the above COFs catalysts, a series of control experiments were carried out on **N-COF*** and **S-COF***. With Ar bubbling for 30 min to eliminate O_2 or in dark, both **N-COF*** and **S-COF*** displayed H_2O_2 photosynthetic rates less than 30 μmol g^{-1} h^{-1}, demonstrating the indispensable process of the photocatalysis of O_2. Then,

ORIGINAL UNEDITED MANUSCRIPT

Downloaded from https://academic.oup.com/nsr/advance-article/doi/10.1093/nsr/nwae177/7679147 by guest on 24 May 2024

photocatalytic water oxidation reaction (WOR) for the H_2O_2 production was studied with Ar in $AgNO_3$ aqueous solution. **N-COF*** and **S-COF*** exhibited photocatalytic activity with H_2O_2 photosynthetic rates of 220 and 150 μmol g^{-1} h^{-1}, respectively (Fig. 6d), and almost no dioxygen was detected under this condition. These results revealed that both photocatalytic WOR and ORR processes of H_2O_2 production existed in the as-synthesized COFs. Moreover, an isotopic experiment to simulate the real system (without $AgNO_3$) was conducted for **N-COF*** and **S-COF*** to verify the as-proposed mechanism of ORR by using $^{18}O_2$ (as an electron acceptor) and $H_2{}^{16}O$ (as an electron donor). $^{18}O_2$ (m/z = 36) was detected in the decomposition product of the reaction between photogenerated H_2O_2 and MnO_2 (Fig. 6f and Fig. S49), indicating the H_2O_2 photosynthesis process from ORR.

As for the H_2O_2 photosynthesis reaction mechanism, there are two possible routes for ORR and for WOR from O_2 and water via $2e^-$ redox process, respectively. One of them is a $2e^-$ two-steps process with hydroxyl radicals ($^{\bullet}OH$) and superoxide anion radicals ($^{\bullet}O_2^-$) as the intermediate species for indirect H_2O_2 generation, and the other is a direct $2e^-$ one-step process. In order to verify the mechanism of the full reaction of H_2O_2 photosynthesis for the above two COFs, *in situ* EPR was conducted using 5,5-dimethyl-pyrroline *N*-oxide (DMPO) as the free-radical spin-trapping agent to detect $^{\bullet}OH$ and $^{\bullet}O_2^-$. As depicted in Fig. 6e and Fig. S50, typical characteristic signals of DMPO-$^{\bullet}OOH$ species and DMPO-$^{\bullet}OH$ species were observed in O_2-saturated water for **N-COF*** and **S-COF*** under Xe lamp irradiation and were both absent in dark condition. It implies that H_2O_2 photosynthesis reaction in this COF system complies with a $2e^-$ two-step process with the participation of $^{\bullet}OH$ and $^{\bullet}OOH$.

A possible mechanism can be proposed to illustrate the photosynthesis of H_2O_2 for the **zyg**-type COFs according to the experimental results. Briefly, referring to **N-COF** the dioxygen is absorbed and gain electrons as well as protons at the TAPB-Me sites to generate $^{\bullet}OOH$ active intermediate. Meanwhile, the H_2O molecule utilizes the holes from the TPA sites to form $^{\bullet}OH$ active intermediate. Then, $^{\bullet}OOH$ and $^{\bullet}OH$ active intermediates simultaneously produce H_2O_2 at **N-COF** and **N-COF***. There is a similar situation referring to **S-COF** and **S-COF*** except that the hole utilization for the H_2O molecule happened at PTZ sites instead of TPA sites. In

ORIGINAL UNEDITED MANUSCRIPT

Downloaded from https://academic.oup.com/nsr/advance-article/doi/10.1093/nsr/nwae177/7679147 by guest on 24 May 2024

addition, the PCSs in the COF structures result in different enhancement of the photocatalytic H_2O_2 production rates.

To further understand the insight of catalytic mechanism and the reason why the catalytic performances are distinct for these COFs, DFT calculations on analyzing the contributions of molecular orbital and the Gibbs free energy of the ORR and WOR processes were conducted. First, the molecular orbital analysis was carried out on the constructed cluster models, revealing that both **N-COF** and **S-COF** present an excellent spatial charge separation in which the HOMO is mainly located in the TPA and PTZ moieties for **N-COF** and **S-COF**, respectively, and the LUMO is dominantly located at the imine and its adjacent phenyl group in the TAPB-Me site (Fig. S51). Thus, we can deduce the reaction pathway as follows: First, during the light activation process of forming the corresponding excitation activation species **N-COF*** and **S-COF*** from **N-COF** and **S-COF**, the electron transfer probably takes place from the TPA or PTZ group to the imine group site and produces the metastable PCSs; second, the photocatalytic reduction reaction occurs around the electron positions (imine sites) and the oxidation reaction at the hole positions (the TPA or the PTZ sites) for **N-COF** and **S-COF**, respectively. Since the excitation process is realized by light irradiation, the metastable radical species after excitation have been captured by experiments. Therefore, the theoretical calculation takes the **N-COF*** and **S-COF*** intermediates after the PCS process as the origination. For comparison, **N-COF** and **S-COF** catalytic potential energy surfaces before excitation are also considered (Fig. 6g). In addition, because **N-COF** and **S-COF** contain the same building unit TAPB-Me, the mechanism of the ORR catalytic process is the same for both. So, there are only two lines on the potential energy surface of the ORR process (red line represents the ground state species for **N-COF**/**S-COF** and blue line represents the excited species for **N-COF***/**S-COF***).

In general, the first process in ORR and WOR is the potential determination step for the photocatalytic two-step H_2O_2 production. Based on the calculation results, when regarding to the ORR process, the O_2 molecules are absorbed at the imine N sites and then experience one electron reduction and protonation to form $^{\bullet}$OOH intermediate. The Gibbs free energy change (ΔG^{o}) values for this process are −2.23 eV for **N-COF**/**S-COF** and −4.63 eV for **N-COF***/**S-COF***, meaning that the ORR is thermodynamically favorable for all these COFs and more energy-favorable for the

ORIGINAL UNEDITED MANUSCRIPT

Downloaded from https://academic.oup.com/nsr/advance-article/doi/10.1093/nsr/nwae177/7679147 by guest on 24 May 2024

excited species **N-COF*/S-COF***. Then one more photogenerated electron and proton transfer into the •OOH intermediate, fulfilling the two-step ORR process from O_2 to H_2O_2 product with ΔG^o values of −3.23 eV and −5.72 eV for **N-COF**/**S-COF** and **N-COF*/S-COF*** relative to initial point, respectively. It reveals that the electron-obtaining status (reductive TAPB-Me species) for the **N-COF** and **S-COF** was more beneficial to the photocatalytic ORR process. When regarding to the WOR process, the H_2O molecules are absorbed at the N atom of TPA for **N-COF**/**N-COF*** and at the phenothiazine ring for **S-COF**/**S-COF***, and one electron oxidation as well as deprotonation subsequently occurs resulting in the generating of •OH intermediate. The ΔG^o values of this step are 2.69 eV and 2.63 eV for **N-COF** and **N-COF***, respectively, which are comparable before and after light activation. By contrast, the free energies of forming •OH intermediate show the distinct energy difference for **S-COF** and **S-COF*** (ΔG^o = 2.32 eV and 0.88 eV), respectively. Two •OH intermediates would desorb and combine to generate H_2O_2, achieving the two-step WOR process with ΔG^o values of 1.19, 1.14, 1.57 and 0.14 eV for **N-COF**, **N-COF***, **S-COF** and **S-COF*** (Fig. 6g), respectively. These results reveal that the electron-donating status was beneficial to the photocatalytic WOR process for the **S-COF** (oxidized PTZ species) while had little effect for the **N-COF** (oxidized TPA species). These calculation results have explained the catalytic performance differences as below: 1) the photocatalytic H_2O_2 production performance was comparable for the ground-state **N-COF** and **S-COF**; 2) the photocatalytic H_2O_2 production performance enhanced for the excited-states **N-COF*/S-COF*** compared with **N-COF**/**S-COF**; 3) the performance enhancement compared to their initial states was much more significant for **S-COF*** than **N-COF***.

CONCLUSION

In summary, we have demonstrated a design strategy of utilizing inequilateral hexagonal building units to prepare 3D COFs (**M-COF**, **N-COF**, **S-COF** and **T-COF**) based on [6 + 4] network with a previously unreported **zyg** topology in COF structures. It is noteworthy that these **zyg**-type COFs exhibit two types of one-dimensional channels and a fascinating fused Olympic ring-like pore shape in the unit cell *c* axis. Both **N-COF** and **S-COF** containing photo-catalytically active groups

ORIGINAL UNEDITED MANUSCRIPT

Downloaded from https://academic.oup.com/nsr/advance-article/doi/10.1093/nsr/nwae177/7679147 by guest on 24 May 2024

showed excellent activity in photosynthesis of H_2O_2 compared to other COF photocatalysts. Subsequently the photochromic radical states for the above two COFs (**N-COF*** and **S-COF***) were successfully obtained, showing dramatic enhancement in the photoactivity for H_2O_2 synthesis compared to the parent materials. Remarkably, **S-COF*** showed H_2O_2 photosynthetic rate of 3324 μmol g^{-1} h^{-1}, >400% enhancement in activity compared to **S-COF**, ranking **S-COF*** as one of the best porous crystalline photocatalysts in overall H_2O_2 photosynthesis. This work provides an effective strategy for constructing PRSs in **zyg**-type 3D COFs, which facilitate the significant photocatalytic activity enhancement for H_2O_2 synthesis. This work would shed light on the development of efficient 3D COF photocatalysts building on the functional organic building blocks assembled in topologies for facilitating the photoinduced charge separation.

SUPPLEMENTARY DATA

Supplementary data are available at *NSR* online.

FUNDING

This work was financially supported by the National Key R&D Program of China (2023YFA1507204) and the National Natural Science Foundation of China (22225109, 22071109 and 22271103).

AUTHOR CONTRIBUTIONS

Y.Y. and Y.-Q.L. conceived the idea. T.-T.M. conducted the synthesis and characterizations for all the samples and interpreted the data. Y.Y. conducted the PXRD refinements and structure analyses. T.-T.M., G.-Z.H., Y.L., B.W., S.-J.Y. and S.-L.L. performed the photocatalytic H_2O_2 synthesis experiments. X.-H.W. and R.-H.L. supported the theoretical analysis of the catalytic mechanisms. Y.Y., T.-T.M. and G.-Z.H. wrote the original draft. Y.Y. and Y.-Q.L. reviewed and edited it. All authors approved the final version of the manuscript.

ORIGINAL UNEDITED MANUSCRIPT

Downloaded from https://academic.oup.com/nsr/advance-article/doi/10.1093/nsr/nwae177/7679147 by guest on 24 May 2024

***Conflict of interest statement*.** None declared.

REFERENCES

1. Yang H, Impano S, Shepard E M *et al.* Photoinduced electron transfer in a radical SAM enzyme generates an S-adenosylmethionine derived methyl radical. *J Am Chem Soc* 2019; **141**: 16117-16124.
2. Mora S J, Odella E, Moore G F *et al.* Proton-coupled electron transfer in artificial photosynthetic systems. *Acc Chem Res* 2018; **51**: 445-453.
3. Kaila V R I. Resolving chemical dynamics in biological energy conversion: long-range proton-coupled electron transfer in respiratory complex I. *Acc Chem Res* 2021; **54**: 4462-4473.
4. Yu X-Q, Sun C, Liu B-W *et al.* Directed self-assembly of viologen-based 2D semiconductors with intrinsic UV–SWIR photoresponse after photo/thermo activation. *Nat Commun* 2020; **11**: 1179.
5. Han S-D, Hu J-X, Wang G-M. Recent advances in crystalline hybrid photochromic materials driven by electron transfer. *Coord Chem Rev* 2022; **452**: 214304.
6. Vermeulen L A, Thompson M E. Stable photoinduced charge separation in layered viologen compounds. *Nature* 1992; **358**: 656–658.
7. Han Y-F, Zhang N-N, Wang M-S *et al.* Achieving different color changes for photochromic compounds by controlling coordination modes. *J Phys Chem C* 2020; **124**: 27680-27686.
8. Mwalukuku V M, Liotier J, Riquelme A J *et al.* Strategies to improve the photochromic properties and photovoltaic performances of naphthopyran dyes in dye-sensitized solar cells. *Adv Energy Mater* 2023; **13**: 2203651.
9. Li L, Yu Y-T, Hua Y *et al.* Recent progress in polyoxometalate–viologen photochromic hybrids: structural design, photochromic mechanism, and applications. *Inorg Chem Front* 2023; **10**: 1965-1985.
10. Cao X, Chen Z, Lin R *et al.* A photochromic composite with enhanced carrier separation for the photocatalytic activation of benzylic C–H bonds in toluene. *Nat*

ORIGINAL UNEDITED MANUSCRIPT

Downloaded from https://academic.oup.com/nsr/advance-article/doi/10.1093/nsr/nwae177/7679147 by guest on 24 May 2024

Catal 2018; **1**: 704-710.

11. Huang G-Z, Lu P-X, Zeng M-M *et al.* Room temperature photochromism and photoinduced slow magnetic relaxation of cyanometallic supramolecular hybrid salts. *J Mater Chem C* 2023; **11**: 5611-5615.
12. Haldar R, Ghosh A, Maji T K. Charge transfer in metal–organic frameworks. *Chem Commun* 2023; **59**: 1569-1588.
13. Wang L, Yang L, Gong L *et al.* Constructing redox-active microporous hydrogen-bonded organic framework by imide-functionalization: Photochromism, electrochromism, and selective adsorption of C_2H_2 over CO_2. *Chem Eng J* 2020; **38**3: 123117.
14. Nie H, Rao Y, Song J *et al.* Through-space conjugated supramolecular polymer radicals from spatial organization of cucurbit[8]uril: an efficient approach for electron transfer and smart photochromism materials. *Chem Mater* 2022; **34**: 8925-8934.
15. Côté A P, Benin A I, Ockwig N W *et al.* Porous, crystalline, covalent organic frameworks. *Science* 2005; **310**: 1166-1170.
16. Geng K, He T, Liu R *et al.* Covalent organic frameworks: design, synthesis, and functions. *Chem Rev* 2020; **120**: 8814-8933.
17. Gong Y-N, Guan X, Jiang H-L. Covalent organic frameworks for photocatalysis: synthesis, structural features, fundamentals and performance. *Coord Chem Rev* 2023; **475**: 214889.
18. Suleman S, Zhang Y, Qian Y *et al.* Turning on singlet oxygen generation by outer-sphere microenvironment modulation in porphyrinic covalent organic frameworks for photocatalytic oxidation. *Angew Chem Int Ed* 2023; **63**: e202314988.
19. Guo J, Xu Y, Jin S *et al.* Conjugated organic framework with three-dimensionally ordered stable structure and delocalized π clouds. *Nat Commun* 2013; **4**: 2736.
20. Chen L, Furukawa K, Gao J *et al.* Photoelectric covalent organic frameworks: converting open lattices into ordered donor–acceptor heterojunctions. *J Am Chem Soc* 2014; **136**: 9806-9809.

ORIGINAL UNEDITED MANUSCRIPT

Downloaded from https://academic.oup.com/nsr/advance-article/doi/10.1093/nsr/nwae177/7679147 by guest on 24 May 2024

21. Feng T, Streater D, Sun B *et al.* Tuning photoexcited charge transfer in imine-linked two-dimensional covalent organic frameworks. *J Phys Chem Lett* 2022; **13**: 1398-1405.
22. Marcus R A. On the theory of electron-transfer reactions. VI. unified treatment for homogeneous and electrode reactions. *J Chem Phys* 1965; **43**: 679-701.
23. Sun J-K, Yang X-D, Yang G-Y *et al.* Bipyridinium derivative-based coordination polymers: from synthesis to materials applications. *Coord Chem Rev* 2019; **378**: 533-560.
24. O'Keeffe M, Peskov M A, Ramsden S J *et al.* The reticular chemistry structure resource (RCSR) database of, and symbols for, crystal nets. *Acc Chem Res* 2008; **41**: 1782-1789.
25. Wang X, Gao F, Kang Z *et al.* Reticular chemistry within three-dimensional covalent organic frameworks for multiple applications. *J Mater Chem A* 2023; **11**: 20368-20382.
26. Wang Y, Liu Y, Li H *et al.* Three-dimensional mesoporous covalent organic frameworks through steric hindrance engineering. *J Am Chem Soc* 2020; **142**: 3736-3741.
27. Arora N, Flores C, Senarathna M C *et al.* Design, synthesis, and applications of mesoporous covalent organic frameworks. *CCS Chem* 2024; **6**: 57-68.
28. Guan X, Chen F, Fang Q *et al.* Design and applications of three dimensional covalent organic frameworks. *Chem Soc Rev* 2020; **49**: 1357-1384.
29. Gui B, Lin G, Ding H *et al.* Three-dimensional covalent organic frameworks: from topology design to applications. *Acc Chem Res* 2020; **53**: 2225-2234.
30. Uribe-Romo F J, Hunt J R, Furukawa H *et al.* A crystalline imine-linked 3-D porous covalent organic framework. *J Am Chem Soc* 2009; **131**: 4570-4571.
31. El-Kaderi H M, Hunt J R, Mendoza-Cortés J L *et al.* Designed synthesis of 3D covalent organic frameworks. *Science* 2007; **316**: 268-272.
32. Lin G, Ding H, Yuan D *et al.* A pyrene-based, fluorescent three-dimensional covalent organic framework. *J Am Chem Soc* 2016; **138**: 3302-3305.
33. Li H, Ding J, Guan X *et al.* Three-dimensional large-pore covalent organic

ORIGINAL UNEDITED MANUSCRIPT

Downloaded from https://academic.oup.com/nsr/advance-article/doi/10.1093/nsr/nwae177/7679147 by guest on 24 May 2024

framework with stp topology. *J Am Chem Soc* 2020; **142**: 13334-13338.

34. Lu H S, Han W K, Yan X *et al.* A 3D anionic metal covalent organic framework with soc topology built from an octahedral TiIV complex for photocatalytic reactions. *Angew Chem Int Ed* 2021; **60**: 17881-17886.
35. Li Z, Sheng L, Hsueh C *et al.* Three-dimensional covalent organic frameworks with hea topology. *Chem Mater* 2021; **33**: 9618-9623.
36. Xu X, Cai P, Chen H *et al.* Three-dimensional covalent organic frameworks with she topology. *J Am Chem Soc* 2022; **144**: 18511-18517.
37. Li X, Gao Q, Aneesh J *et al.* Molecular engineering of bandgaps in covalent organic frameworks. *Chem Mater* 2018; **30**: 5743-5749.
38. Wang W, Wang H, Tang X *et al.* Phenothiazine-based covalent organic frameworks with low exciton binding energies for photocatalysis. *Chem Sci* 2022; **13**: 8679-8685.
39. Liu Y, Jiang X, Chen L *et al.* Rational design of a phenothiazine-based donor–acceptor covalent organic framework for enhanced photocatalytic oxidative coupling of amines and cyclization of thioamides. *J Mater Chem A* 2023; **11**: 1208-1215.
40. Guo Z, Wu H, Srinivas G *et al.* A metal–organic framework with optimized open metal sites and pore spaces for high methane storage at room temperature. *Angew Chem Int Ed* 2011; **50**: 3178-3181.
41. Mishra B, Alam A, Kumbhakar B *et al.* Impact of the crystallinity of covalent organic frameworks on photocatalytic hydrogen evolution. *Cryst Growth Des* 2023; **23**: 4701-4719.
42. Chen Z, Yao D, Chu C *et al.* Photocatalytic H_2O_2 production systems: design strategies and environmental applications. *Chem Eng J* 2023; **451**: 138489.
43. Nouar F, Eubank J F, Bousquet T *et al.* Supermolecular building blocks (SBBs) for the design and synthesis of highly porous metal-organic frameworks. *J Am Chem Soc* 2008; **130**: 1833-1835.
44. Yan Y, Lin X, Yang S *et al.* Exceptionally high H_2 storage by a metal–organic polyhedral framework. *Chem Commun* 2009; 1025–1027.

ORIGINAL UNEDITED MANUSCRIPT

Downloaded from https://academic.oup.com/nsr/advance-article/doi/10.1093/nsr/nwae177/7679147 by guest on 24 May 2024

45. Yuan D, Zhao D, Sun D *et al.* An isoreticular series of metal–organic frameworks with dendritic hexacarboxylate ligands and exceptionally high gas-uptake capacity. *Angew Chem Int Ed* 2010; **49**: 5357-5361.
46. Yong Z, Ma T. Solar-to-H_2O_2 catalyzed by covalent organic frameworks. *Angew Chem Int Ed* 2023; **62**: e202308980.
47. Li Q, Jiao Y, Tang Y *et al.* Shear stress triggers ultrathin-nanosheet carbon nitride assembly for photocatalytic H_2O_2 production coupled with selective alcohol oxidation. *J Am Chem Soc* 2023; **145**: 20837-20848.
48. Zhao Y, Zhang P, Yang Z *et al.* Mechanistic analysis of multiple processes controlling solar-driven H_2O_2 synthesis using engineered polymeric carbon nitride. *Nat Commun* 2021; **12**: 3701.
49. Krishnaraj C, Sekhar Jena H, Bourda L *et al.* Strongly reducing (diarylamino)benzene-based covalent organic framework for metal-free visible light photocatalytic H_2O_2 generation. *J Am Chem Soc* 2020; **142**: 20107-20116.
50. Liao Q, Sun Q, Xu H *et al.* Regulating relative nitrogen locations of diazine functionalized covalent organic frameworks for overall H_2O_2 photosynthesis. *Angew Chem Int Ed* 2023; **62**: e202310556.

ORIGINAL UNEDITED MANUSCRIPT

Downloaded from https://academic.oup.com/nsr/advance-article/doi/10.1093/nsr/nwae177/7679147 by guest on 24 May 2024

Figure Captions

Figure 1. Schematic representation of photoinduced charge separation of D-A pairs in 3D framework (a) and the 3D COFs constructed from 4-connected and 6-connected building blocks (b). Different from the reported [6 + 4] topologies, the **zyg** net can provide a platform for producing obstructive photoinduced charge separation radial pairs.

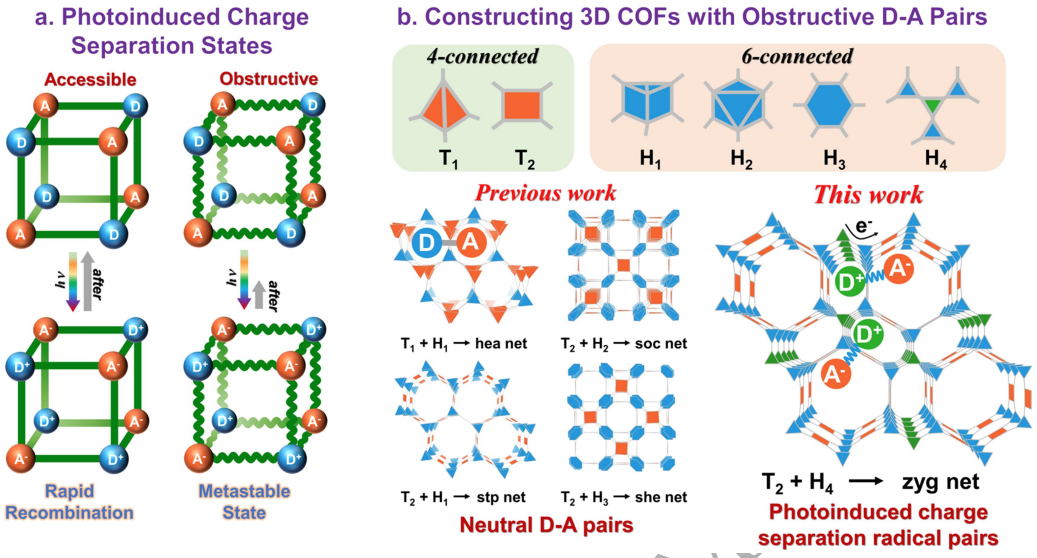

ORIGINAL UNEDITED MANUSCRIPT

Downloaded from https://academic.oup.com/nsr/advance-article/doi/10.1093/nsr/nwae177/7679147 by guest on 24 May 2024

Figure 2. Structures and characterizations of **M-COF**, **N-COF**, **S-COF** and **T-COF**. (Columns b, c, d from top to bottom are in the order of **M-COF**, **N-COF**, **S-COF** and **T-COF**). (a) Synthesis of COFs using the hexa-aldehyde and tetramine precursors. (b) Extended structures of COFs viewed along the crystallographic *c* axis. (c) PXRD patterns and Pawley refinements of the unit cell parameters based on the crystal structure models. (d) N_2 adsorption−desorption isotherms and pore size distributions.

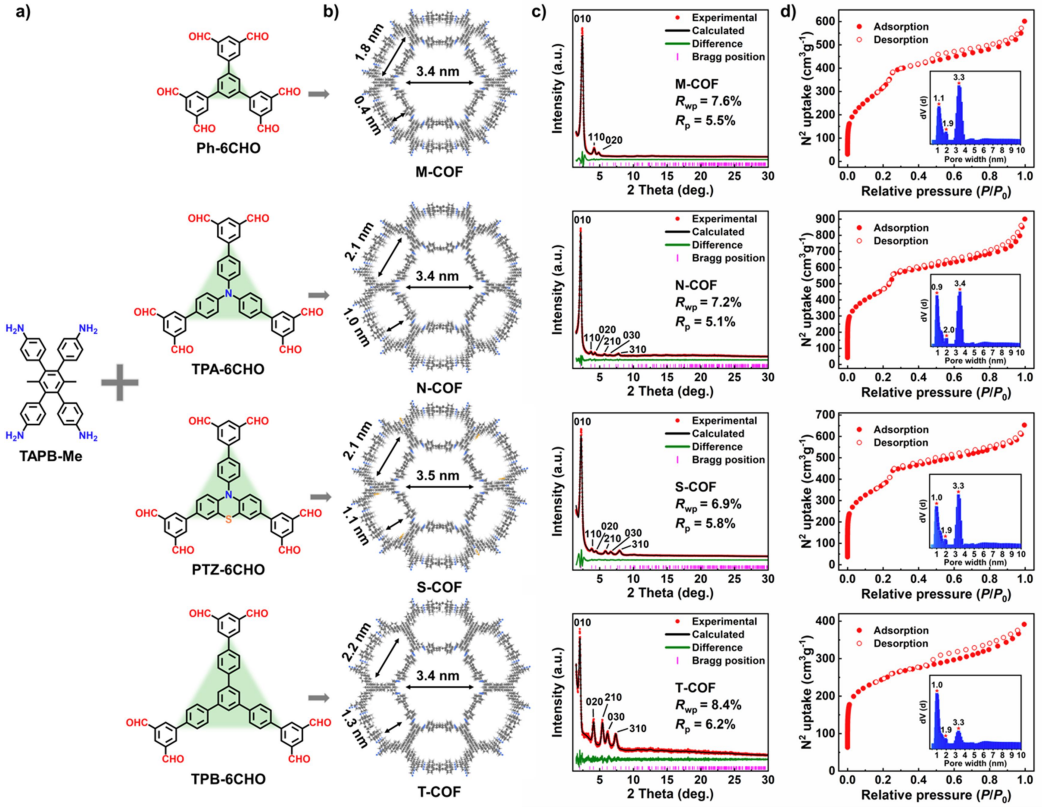

ORIGINAL UNEDITED MANUSCRIPT

Downloaded from https://academic.oup.com/nsr/advance-article/doi/10.1093/nsr/nwae177/7679147 by guest on 24 May 2024

Figure 3. Electron microscopy images of the as-synthesized COFs. (a) SEM image of **N-COF**. A hexagonal crystal is marked with the red hexagon. (b) TEM image of **N-COF** and (c) its IFFT. The magnified region in the area marked with the red box in the IFFT image for **N-COF** (c) and overlay of the structure model along [001] direction (d). TEM images of (e) **M-COF** and (f) **S-COF**.

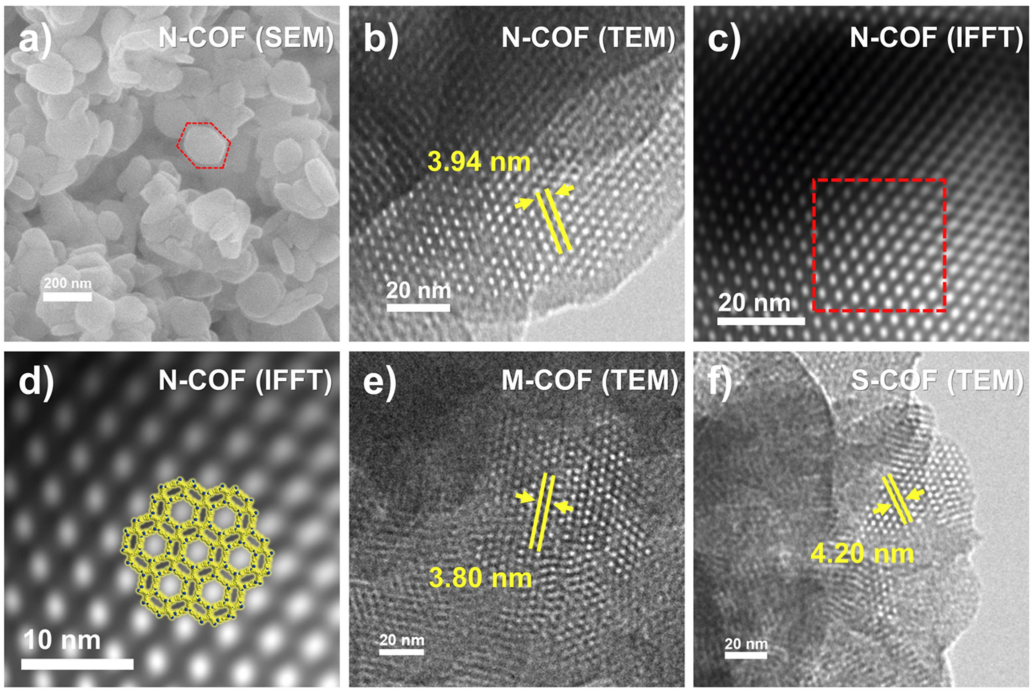

ORIGINAL UNEDITED MANUSCRIPT

Downloaded from https://academic.oup.com/nsr/advance-article/doi/10.1093/nsr/nwae177/7679147 by guest on 24 May 2024

Figure 4. Structure of the Fusion Olympic Rings-shaped framework and the two different channels in the **zyg**-type COFs exemplified by **M-COF**. (a) Single and multi-layer aperture maps for smaller hexagons (channel A). (b) Extended structure of **M-COF** viewed along the *c* axis and fused five-member rings derived from Olympic rings. (c) Single and multi-layer aperture maps for larger hexagons (channel B).

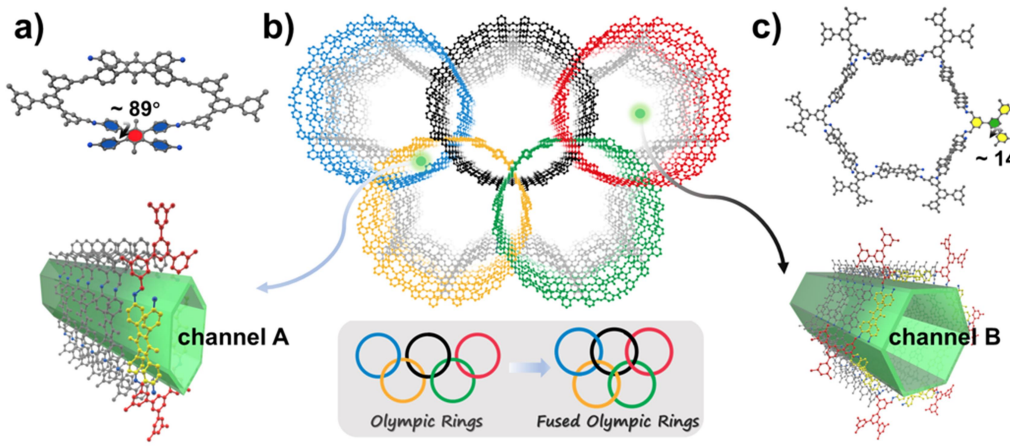

ORIGINAL UNEDITED MANUSCRIPT

Downloaded from https://academic.oup.com/nsr/advance-article/doi/10.1093/nsr/nwae177/7679147 by guest on 24 May 2024

Figure 5. (a) EPR spectra for the irradiated samples of as-prepared **zyg**-type COFs in the solid state. (b) EPR spectra for the irradiated samples of as-prepared **zyg**-type COFs under the catalytic reaction condition. (c) UV-Vis DRS for **N-COF** and **S-COF** and their activated states (inset: photographs of the COF powders). (d) T_{auc} plots for band gap calculations. (e) Transient photocurrent response and (f) band-structure diagram for **N-COF**, **S-COF**, **N-COF*** and **S-COF***.

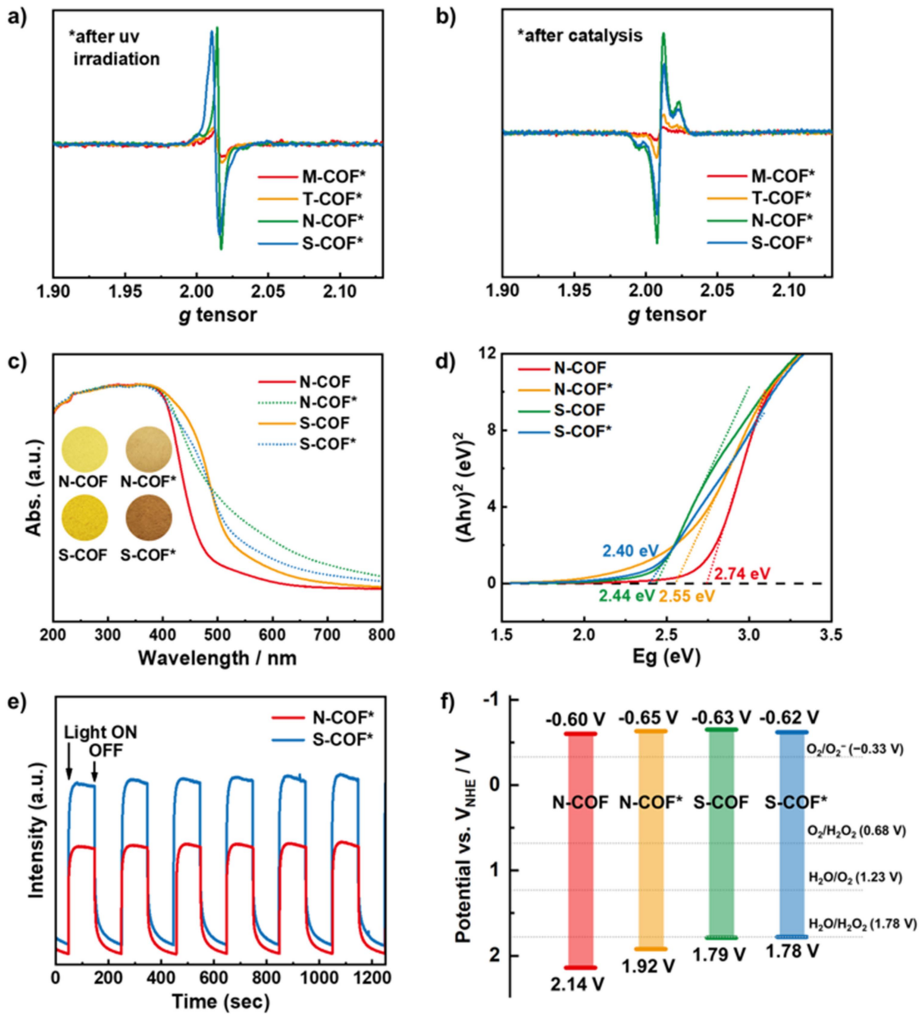

ORIGINAL MANUSCRIPT

Downloaded from https://academic.oup.com/nsr/advance-article/doi/10.1093/nsr/nwae177/7679147 by guest on 24 May 2024

Figure 6. (a) Photocatalytic H_2O_2 production rates of **N-COF, S-COF, N-COF*** and **S-COF*** in pure water and 10% isopropanol aqueous solution. (b) Time-dependent photocatalytic activity of **N-COF, S-COF, N-COF*** and **S-COF*** for H_2O_2 production in pure water. (c) Cycling tests over **N-COF*** and **S-COF*** for the photocatalytic H_2O_2 production from O_2 and H_2O. (d) Single-variable control experimental tests of the photocatalytic H_2O_2 production performance for **N-COF*** and **S-COF*** under different conditions. (e) EPR spectra of the reaction solution under the dark and visible light illumination for **S-COF*** in the presence of DMPO as the spin-trapping reagent. (f) $^{18}O_2$ isotope experiment in order to identify the source of O in H_2O_2. (g) Free energy diagram of H_2O_2 photosynthesis through the ORR and WOR pathways for **N-COF, S-COF, N-COF*** and **S-COF*** and the key steps of H_2O_2 photosynthesis mechanism.

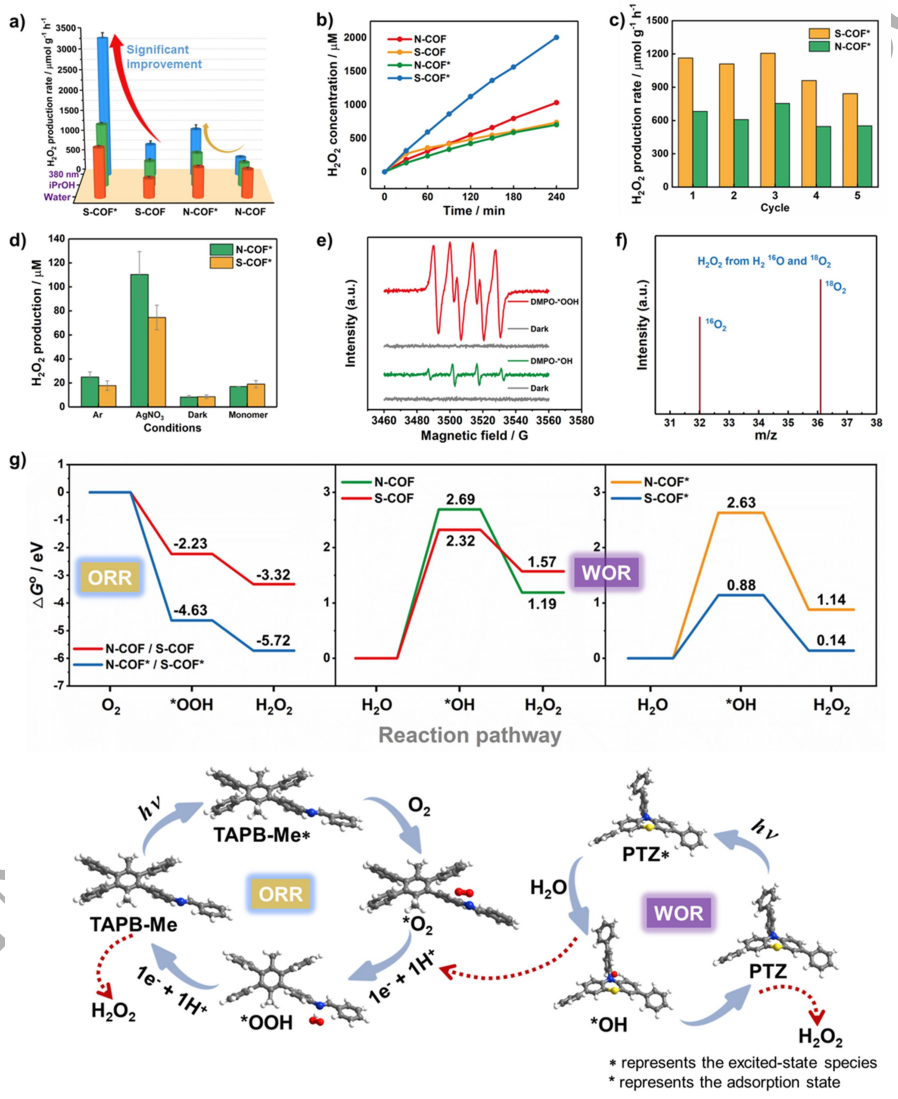

ORIGINAL MANUSCRIPT

Downloaded from https://academic.oup.com/nsr/advance-article/doi/10.1093/nsr/nwae177/7679147 by guest on 24 May 2024